DTU Library

Correlative study of liquid in human bone by 3D neutron microscopy and lab-based X-ray µCT

Østergaard, Maja; Naver, Estrid Buhl; Schüpbach, Delia; Kaestner, Anders; Strobl, Markus; Brüel, Annemarie; Thomsen, Jesper Skovhus; Schmidt, Søren; Poulsen, Henning Friis; Kuhn, Luise Theil

Total number of authors:
11

[Link back to DTU Orbit](#)

Full Length Article

Correlative study of liquid in human bone by 3D neutron microscopy and lab-based X-ray µCT

Maja Østergaard [a], Estrid Buhl Naver [b], Delia Schüpbach [c], Anders Kaestner [c], Markus Strobl [c,d], Annemarie Brüel [e], Jesper Skovhus Thomsen [e], Søren Schmidt [f], Henning Friis Poulsen [g], Luise Theil Kuhn [b], Henrik Birkedal [a,*]

[a] Department of Chemistry and iNANO, Aarhus University, Aarhus, Denmark
[b] Department of Energy Conversion and Storage, Technical University of Denmark, Kongens Lyngby, Denmark
[c] Laboratory for Neutron Scattering and Imaging, Paul Scherrer Institute, Villigen, Switzerland
[d] Niels Bohr Institute, University of Copenhagen, Copenhagen, Denmark
[e] Department of Biomedicine, Aarhus University, Aarhus, Denmark
[f] Data Management and Software Centre, European Spallation Source, Lund, Sweden
[g] Department of Physics, Technical University of Denmark, Lyngby, Denmark

ARTICLE INFO

ABSTRACT

Liquid plays an important role in bone that has a complex 3D hierarchical pore structure. However, liquid (water) is difficult to discern from *e.g.* an organic matrix by X-ray imaging. Therefore, we use a correlative approach using both high resolution X-ray and neutron imaging. Human femoral bone with liquid adsorbed into some of the pores was imaged with both the Neutron Microscope at the ICON beamline, SINQ at PSI, and by lab-based µCT using 2.7 µm voxel size. Segmentation of the two datasets showed that, even though the liquid was clearly distinguishable in the neutron data and not in the X-ray data, it remained challenging to segment it from bone due to overlaps of peaks in the gray level histograms. In consequence, segmentations from X-ray and neutron data varied significantly. To address this issue, the segmented X-ray porosities was overlaid on the neutron data, making it possible to localize the liquid in the vascular porosities of the bone sample and use the neutron attenuation to identify it as H_2O. The contrast in the neutron images was lowered slightly between the bone and the liquid compared to the bone and the air. This correlative study shows that the complementary use of X-rays and neutrons is very favorable, since H_2O is very distinct in the neutron data, while D_2O, H_2O, and organic matter can barely be distinguished from air in the X-ray data.

1. Introduction

Bone is a hierarchical composite material composed mainly of collagen, nanocrystalline apatite, and water [1–6]. It is replete with a porous network of blood vessels and cells, which are housed in lacunae that are interconnected by canaliculi [7]. The cells in the bone are responsible for the bone remodeling, which is a process where old bone is replaced with new. The lacuno-canalicular network in bone is filled with fluid, which contains ions and nutrients important for the function of bone [6,8–10]. To understand for example, how intercellular communication works in bone or how bone remodeling process is initiated; we need to study the complex porous network of large canals, smaller channels, and all the way down to the cellular level and the transport of liquid herein.

Imaging is a great tool for visualizing complex hierarchical structures, like bone, as it directly shows the structure in question by providing spatially resolved information even in 3D with computed tomography. X-rays are the most common imaging modality used to study bone, since it is readily available and provides excellent contrast between mineralized tissue, soft tissue, and air. With absorption as contrast mechanism, X-rays are highly sensitive to the material density, which allow for distinguishing between different levels of

mineralization of bone. However, in some cases, X-rays are not the optimal modality option for imaging bone samples. Metal implants in bones often introduce artifacts in the resulting images because metal is much denser than mineralized bone. Here, neutron imaging would be preferable, as the neutron interaction cross sections do not scale with atomic number, and neutrons are therefore less sensitive to the much denser metal implants [11–15]. In addition, neutrons are sensitive to the isotope composition, so there is potential to control the image contrast this way. This is useful when exploring liquid transport in various materials [16–18] and will be utilized in this study to identify the type of liquid.

The contrast of water is also part of the scope of this article, as a piece of bone was imaged with neutron microscopy after D_2O uptake experiments [19]. As X-rays and neutrons interact differently in the inspected materials, the information obtained from X-ray and neutron imaging will be different. Thus, a comparative study using both X-rays and neutrons can be advantageous, especially for materials that display different contrast in the two modalities, like water [14–16,20]. Combining the information gathered by X-rays and neutrons has previously been performed for studying bone [13,21,22], but advances in this field can be beneficial and make correlative neutron and X-ray even more powerful.

Previous studies of bone by neutron imaging have used relatively large voxel sizes so that vascular canals were not visible. For example, Schwarz et al. [21] used 272 μm voxel size to study vertebrate remains, Törnquist et al. [13] made use of the fact that metals generally (but not always) absorb neutrons less than for X-rays to avoid metal artifacts in a study of the bone/implant interface with a 18.6 μm voxel size. Törnquist et al. [20] showed that the degree of hydration of bone by heavy water impacts the attainable contrast-to-noise ratios on rat tibiae and trabecular bovine bone plugs using a 7.15 μm voxel size; vascular spaces within the cortical bone was not visible in the presented data. Silveira et al. [16] compared uptake of D_2O with H_2O-wet samples of fish bone with and without osteocytes. They used an effective voxel size of 7.6 μm, which meant osteocyte lacunae were indetectable; no vascular signatures are visible in the published images. The authors used differential imaging (difference between images of D_2O and H_2O containing samples) to quantify the D_2O uptake and thereby elegantly obtain a measure of the water permeability in the bones even if the porosity behind it was not directly observed. These previous works highlight several advantages of the different contrast mechanisms between X-ray and neutron imaging but did not resolve vascular spaces. In the present study, we therefore investigate human femoral bone using both X-ray and neutron microscopy with a 2.7 μm voxel size that allows detecting vasculature in both imaging modalities. We will highlight the contrast differences of H_2O in the porosities of bone when measured with neutron microscopy compared to lab-based X-ray microscopy. In addition, we will highlight the advantages of dual modality imaging and show that correlative analysis of the two image modalities affords deeper insights into the material than either on their own.

2. Experimental

2.1. Bone samples

Human bone was obtained from the Body Donation Program at Department of Biomedicine, Aarhus University. Required permission was obtained from the Scientific Ethical Board of the Region of Central Denmark (1-10-72-113-15).

A rod (Ø = 5 mm) was obtained from the shaft of a human femur and prepared so that the vascular canals were mainly oriented along the length of the cylindrical sample. The rod was obtained by drilling a frozen piece of femoral bone with a trepan. Then, the rod was prepared in a cylindrical shape with semi-parallel ends using a water-cooled band saw equipped with a diamond blade (Exakt Apparatebau GmbH, Norderstedt, Germany). In the body, the water content of bone is around 20

% (by volume) [23], but the sample was kept dry until it was partially infused with D_2O (Eurisotop) while in a custom-built sample holder using a pump (~1 mL/h) (see [19]) and after a considerable amount of time imaged by 3D neutron microscopy. In between D_2O infusion and imaging, the sample was kept dry and in air and can thus be considered dry, except for the possible adsorbed/infused water, when imaged. Thereafter, the sample was stored in air until it was reimaged by 3D X-ray microscopy. We chose this approach to explore the capability of combined X-ray and neutron 3D microscopy to identity the type of liquid in the sample.

2.2. Neutron microscopy

High-resolution 3D absorption-based neutron microscopy [24] data were collected from a bone sample with pores previously infused with D_2O. A tomographic dataset was collected at the Imaging with COld Neutrons (ICON) beamline [25] at the Swiss Spallation Neutron Source (SINQ), Paul Scherrer Institute (PSI). The sample was placed 5 mm from the detector and a white neutron beam ($L/D = 342$, L: distance from collimating pinhole to sample, D: diameter of collimating pinhole) was used to collect 625 projections covering 360°. Each projection was collected with an exposure time of 90 s, repeated 4 times, and averaged before reconstruction giving a total acquisition time of 65 h. In this time, no efforts were made to isolate the sample from the environment so that the bone was considered to be 'dry' except for the infused D_2O, that could isotope exchange to H_2O by interaction with water in the atmosphere, and/or possible adsorbed water. The combination of a $^{157}Gd_2O_2S$:Tb scintillator screen, a magnifying lens, and a CCD camera (Andor Technologies iKon L) resulted in an isotropic voxel size of 2.7 μm.

The neutron data were corrected with open beam data (white image) and dark current data and they were dose corrected [26–28]. Ring removal was conducted using wavelet ring removal [29], after which outlier removal was conducted prior to reconstruction using the filtered back-projection algorithm and a Hamming filter [28]. All these steps were performed in MuhRec [28]. The data were then filtered using the inverse scale space (ISS) filter [30] using total variation regularization in the processing tool KipTool [31]. Further image analysis was carried out in MATLAB (v9.11.0.1837725 (R2021b), MathWorks Inc., MA, USA) and Dragonfly (v2021.3, Object Research Systems (ORS) Inc., Montreal, Canada). A sigmoidal fit of several sample edges in several slices was performed. A mean of all the distances between 10 % and 90 % of the fitted sample edges was used as an estimate of image resolution. Before the thickness mesh calculation and renderings, the neutron data were segmented in Dragonfly. Three segmentations, tentatively assigned to air, bone, or liquid, were obtained after thresholding at gray levels 1.4 cm^{-1} and 3.5 cm^{-1} The two binary volumes corresponding to air and liquid were morphologically opened and closed with a series of sphere kernels starting at 3 voxels and ending at 9 voxels. This removed both the small features and the holes in the segmentations stemming from noise. Then the two segmentations were merged and the air outside the sample was digitally removed. From this data stack, containing both air and liquid filled porosities, renderings were performed and a thickness mesh could be calculated.

2.3. X-ray microscopy

The bone sample was investigated by X-ray micro tomography using a Xradia 620 Versa X-ray microscope (ZEISS, Germany) with a LE2 (low energy) filter, a power of 4.5 W, and an accelerating voltage of 50 kV. With an exposure time of 12 s, 3201 projections were collected while rotating the sample 360°. An optical magnification of ×0.4 and no pixel binning was used to match the neutron microscopy voxel size of 2.7 μm. The source-to-sample distance was 10 mm and the sample-to-detector distance was 116 mm. The reconstructions were conducted with TXM Reconstructor Scout-and-Scan software (v16.1.13038, ZEISS, Germany)

using a cone beam adapted filtered back projection (FBP) algorithm with a beam hardening constant of 0.15 and scaling bounds [−0.1; 0.4]. Since the sample was placed close to the source and the machine has a cone beam, cone angle effects affected a significant part of the field of view. Therefore, two scans were obtained with an overlap of 70 % and subsequently stitched together with the Scout-and-Scan software (ZEISS, Germany). Each scan took 13 h, resulting in a total measurement time of 26 h. The start and end slices of the stack were carefully chosen to match

the start and end slices in the neutron stack and this neutron-matched data were retained for further analysis. To align the neutron and X-ray data, both 3D data sets were placed with the center-of-mass in the center of a zero-padded stack. Then, the X-ray 3D data were rotated using the *imregtform*-function of MATLAB in steps of 1° in the x,y-plane (transverse to the beam direction) and 0.2° in the z,y- and x,z-planes (longitudinally to the beam direction) to find the best rotation and tilt angles as evaluated by image difference. To match the neutron data completely, the X-
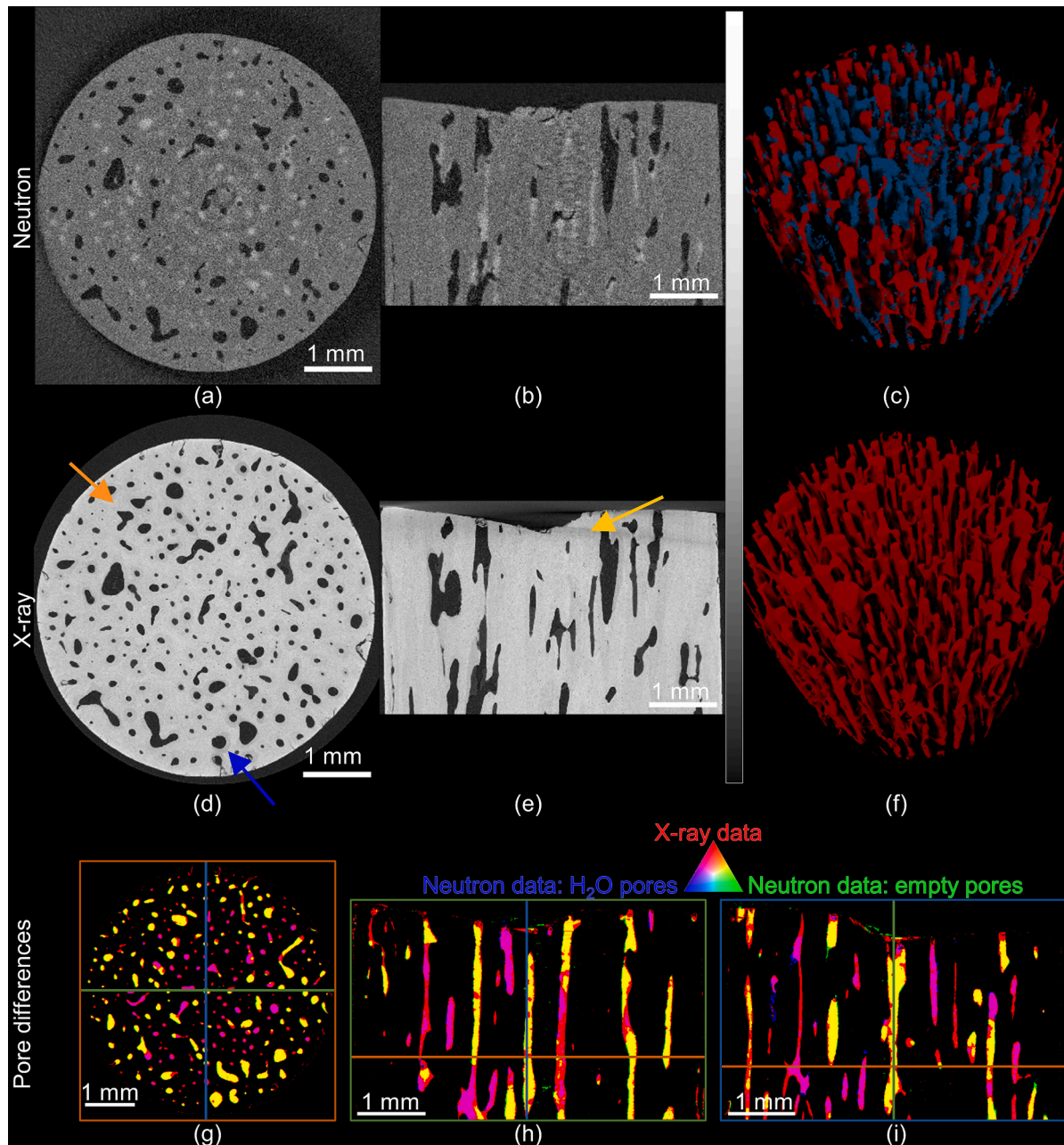

Fig. 1. Neutron microscope and X-ray data. **(a)** Transverse and **(b)** longitudinal virtual slices of neutron microscopy data. Black holes are pores without liquid and light gray holes are pores with liquid. Gray levels range from −1 cm^{-1} to 7 cm^{-1}. **(c)** 3D rendering of the segmented pores of the neutron microscopy data. Blue pores are filled with H_2O, while red pores are empty. **(d)** Transverse and **(e)** longitudinal virtual slices of X-ray microscopy data. The blue arrow indicates osteonal bone, while the orange arrow indicates interstitial bone. Note the cone angle artifacts at the top of (e) indicated with yellow arrow. Gray levels ranges from 5000 a.u. to 60,000 a.u. The X-ray data stack has been rotated, tilted, and scaled to match neutron microscopy data. **(f)** 3D rendering of the segmented vascular porosities in the X-ray microscopy data. Note that the difference in gray level ranges is a result of completely different contrast mechanisms in the datasets, and therefore the gray level values cannot be compared. **(g)** Typical transverse and **(h,i)** longitudinal virtual slices of overlaid pore segmentations as detected by neutrons and X-rays, respectively, displayed as RGB images. The segmentation of the X-ray data is depicted in red, the segmentation of the neutron data for the empty pores in green, and the segmentation for the H_2O filled pores in blue. Slices contain both combinations of aforementioned base colors and the base colors them self. (For interpretation of the references to color in this figure legend, the reader is referred to the web version of this article.)

ray data were downscaled by a factor of 1.0226. After this, we used a custom-made function to scan through the slices in all three dimensions of the X-ray data to match the respective neutron data slices and shifted the X-ray data stack accordingly. Then, the data were upsampled by a factor of four in order to ascertain the best rotation and tilt angles, this time with steps of 0.2° in all three dimensions. After a successful alignment of the X-ray data to match the neutron data, both datasets were segmented using MATLAB, and exported to Dragonfly for rendering and calculation of a thickness mesh.

3. Results

The sample originate from the femoral shaft and therefore consists purely of compact (cortical) bone, so the only void spaces visible at this resolution originate from blood vessels (Fig. 1). Additionally, bone contains an interconnected cellular network, not observed at this resolution [7,32]. The bone sample was imaged with neutron microscopy after the D_2O uptake experiments [19]. Fig. 1a–c presents virtual slices and a 3D rendering of the neutron images. Inspecting the virtual slices in Fig. 1a–b it is possible to observe voids with both lower and higher attenuation contrast than the surrounding bone. These correspond to vascular canals filled with air or liquid, respectively. The liquid initially infused in the bone porosities was D_2O, however the higher contrast of the liquid compared to bone (Fig. 1a–b) suggests H_2O and not D_2O in the porosities. This is ascribed to isotope exchange of D_2O by H_2O by interaction with water in the atmosphere and/or condensation of atmospheric water in the pore space. Due to the contrast between H_2O and bone in this measurement, it is possible to segment the empty canals (red in Fig. 1c) and the canals containing H_2O (blue in Fig. 1c). This required using either morphological operations (see Experimental), more crude smoothing methods or similar. After these additional post-processing steps, the resulting segmentation lacks some of the pore space found in the X-ray segmentation (Fig. 1g–i), which is further discussed below. The neutron gray level histogram (Fig. 2a) displays four separate distributions (Supplementary Fig. 1): two distributions around zero cm^{-1},

which both correspond to air/background (the two different background gray levels in Fig. 2a) and two distributions around 2.5 cm^{-1}, which correspond to either bone or H_2O. However, the last two peaks are not clearly discernible in the histogram (Fig. 2a). Consequently, the bone and H_2O peaks must partially overlap. This testifies to the need for additional post processing steps to analyze the distribution of air/water in the pore spaces fully. The high contrast of the H_2O containing pores reflect that H_2O was indeed infused into the bone in the experiment. However, due to the overlapping distributions (Fig. 2a), it cannot be excluded that the H_2O had partially infused into the bone matrix itself, which would mean that the high contrast signal would represent not only pores but also deuterated bone matrix. Below we will apply correlative X-ray/neutron analysis and show that the H_2O was localized to the pores within the resolution of the measurements.

X-ray microscopy was performed several months after the D_2O uptake experiments in order to allow the sample to dry. Hence, we assume that the sample does not contain any D_2O or H_2O. However, we would not be able to identify D_2O conclusively using X-rays. Indeed, in the histogram (Fig. 2b), a peak is visible around 2×10^4 as a shoulder at slightly higher absorption contrast than air. This peak corresponds to a material that is denser than air, but less dense than mineralized bone. Therefore, it must correspond to some organic residues in the bone, H_2O, or D_2O. This reflects the relative low ability of X-rays to distinguish low-Z materials compared to neutrons, where isotope contrast achieves this with ease. Thus, for the X-ray microscopy data, only one segmentation was performed, separating air/organic/water from bone. This segmentation will be used for correlative analysis of the neutron microscopy data below. The vascular spaces are clearly seen in transverse and longitudinal virtual slices through the bone (Fig. 1d and e) due to the high contrast between air and bone matrix, illustrating how easy these two material phases can be separated (Fig. 1g–i). Therefore, it is evident that more information can be gained from the data, if the X-ray segmentation is combined with the neutron data, where liquid information is easily available. In the X-ray data, the vascular pores are surrounded by newer, less mineralized osteonal bone (blue arrow in Fig. 1d), which has a lower

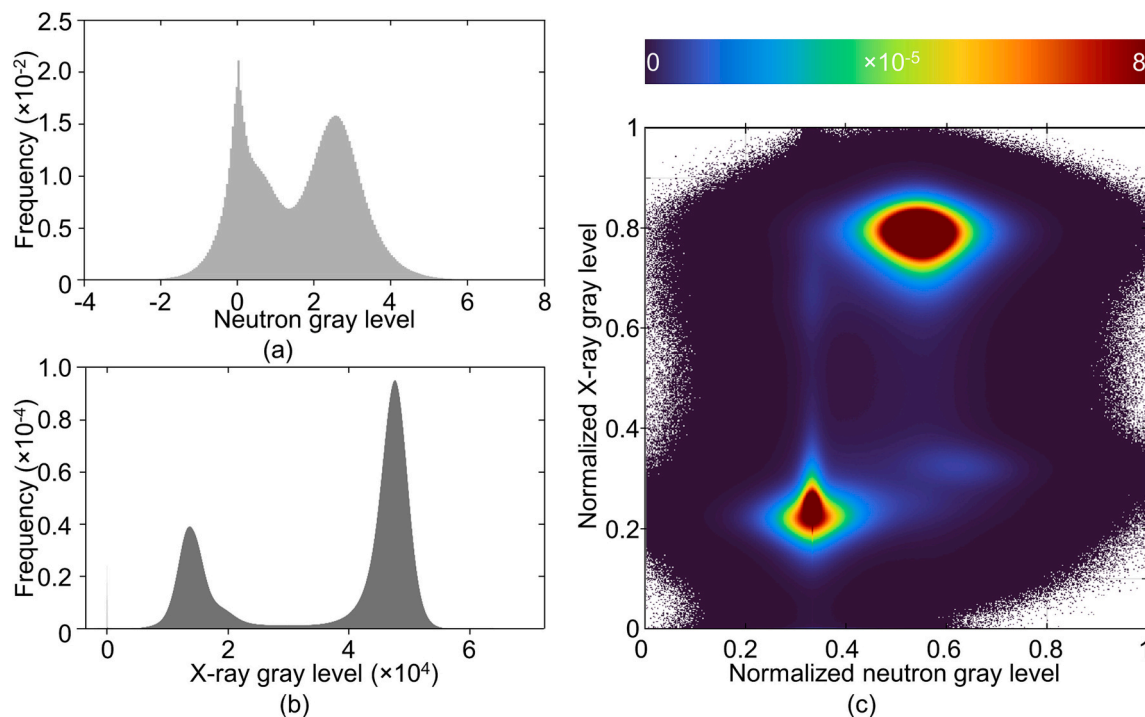**Fig. 2.** Histograms of the gray levels of **(a)** ISS filtered neutron microscopy attenuation data in units of cm^{-1} and **(b)** X-ray microscopy data. Bin width is 0.05 for neutron data and 1 for X-ray data. Note that the gray levels cannot be compared between the two histograms. **(c)** Bi-variate histogram of normalized neutron and X-ray gray levels. Bin width is 0.002 in both directions.

mineral density than the older more mineralized interstitial bone found between the osteonal bone (orange arrow in Fig. 1d), see [33] and references therein. The difference between osteonal bone and interstitial bone is clearly discernable in the X-ray data, in both Fig. 1d–e and in Fig. 2b as a shoulder, reflecting the high sensitivity of X-rays to the concentration of heavy elements (here the calcium and phosphorous in the bone apatite-like mineral) rising with the atomic number Z as Z^4. However, it should be emphasized that this clear distinction between high and low mineral content is made possible by the long measurement time in the present experiment (~26 h); a standard lab-based µCT

measurement would not clearly display the mineralization differences. The segmented pore space is shown in Fig. 1c. We note that the gray values of the X-ray and neutron histograms in Fig. 2 cannot be directly compared since they are results of different probe-sample interaction mechanisms. In addition, the results from the two experiments are shown on different scales. The X-ray data has arbitrary values while the neutron data has values resembling the attenuation coefficient of the probed material. The neutron data is stored as 32-bit floating-point values, while the X-ray data is stored as 16-bit unsigned integers, already here creating a difference in the data range between the two
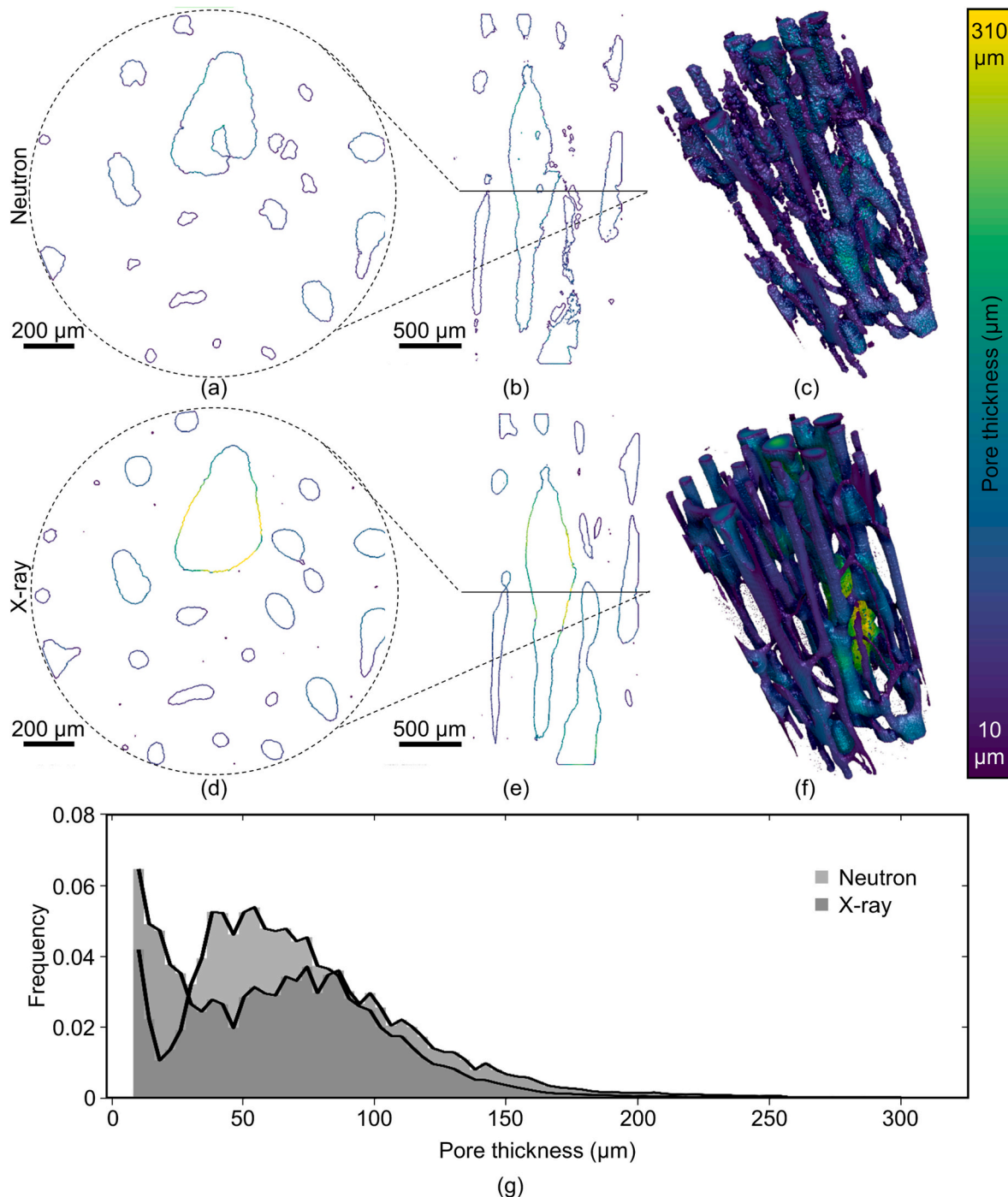
Fig. 3. Pore thickness based on the two segmentations. **(a)** Transverse and **(b)** longitudinal virtual slice of a sub-volume of the thickness mesh from the neutron segmentation. **(c)** 3D rendering of sub-volume of thickness mesh from the neutron segmentation. **(d)** Transverse and **(e)** longitudinal virtual slice of a sub-volume of thickness mesh from the X-ray segmentation. **(f)** 3D rendering of sub-volume of thickness mesh from X-ray segmentation. **(g)** Histogram of the pore thickness from the two segmentations. The bin width is 4 µm.

data sets. In addition, the X-ray data is manually scaled through the choice of gray level window of data to be reconstructed. Thus, even though the neutron histogram in Fig. 2 appears to span fewer gray levels than the corresponding X-ray histogram, this is incorrect. The two datasets were scaled differently and were retained on their respective gray scales during all analyses.

The X-ray data were easily segmented to air and bone, as these two peaks do not overlap in the histogram (Fig. 2b). However, segmenting the neutron data is a bigger challenge, as the peaks for air, bone, and liquid overlap in the histogram (Fig. 2a). Using morphological openings and closings, a segmentation was obtained (Fig. 1c) that resembled the segmentation obtained from the X-ray data (Fig. 1f). From these two segmentations, the pore spaces were obtained. In the segmented X-ray data, 7.9 % of the voxels are labelled as pores, whereas the segmented neutron data (filled with either air or liquid) labelled only 5.6 % of the voxels as pores. This difference between the two segmentations is clearly visible in Fig. 1g–i. In order to obtain insights into the location and/or origin of the difference between the two segmentations, a thickness mesh was calculated to quantify the local extend of the porosities. In general, the pores in the neutron segmentation appear thinner than the pores in the X-ray segmentations (Figs. 3a–f and 1g–i). This is supported by the pore thickness histograms, which show that the pore thickness in the X-ray segmentation peaks at a higher value (median: 66.6 μm) than

the neutron segmentation (median: 61.3 μm) (Fig. 3g). A paired *t*-test (MATLAB), established that the resulting thickness measures were significantly different ($p < 0.001$). Even though the sample is the same in the two measurements, the segmentations separating bone from pore space does not result in the same pore volumes. Thus, this proves the benefits of having a correlative study with two modalities complementing each other.

In order to visualize the liquid in the pores, the neutron data were overlaid with the segmented X-ray data to mask the putative pore space in the neutron data (Fig. 4a–b). A histogram of the intensity in the segmented pores is shown in light gray (Fig. 4g). Two separate peaks (see Supplementary Fig. 2) are present in the pore gray level histogram, corresponding to liquid and air, indicating an easy segmentation between these two, following the use of the X-ray segmentation as a mask. A histogram of the neutron data masked by the bone volume identified by X-ray segmentation is included in dark gray (Fig. 4g). This histogram presents a single peak at a gray level between the air and liquid peaks in the unmasked neutron data histogram. Again, the higher attenuation of the liquid compared to bone indicates that the liquid is H_2O rather than D_2O and as the liquid gray value distribution (Fig. 4g) peaks around 3.5 cm^{-1}, we can indeed assign the liquid to be H_2O in the porosities [34–36]. The D_2O has isotope exchanged to H_2O between the infusion and measurement time, since the sample has been stored without any
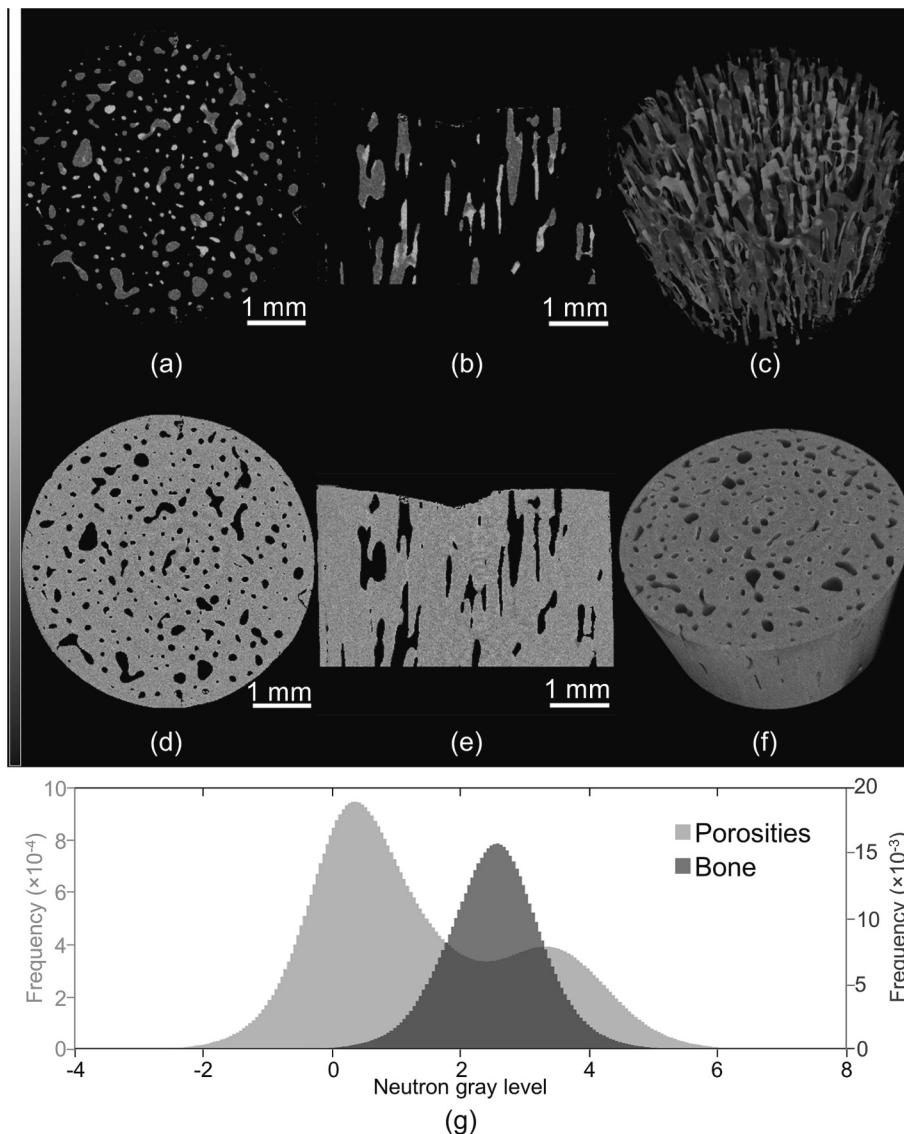

Fig. 4. Filtered neutron microscope data masked with X-ray data segmentation. **(a)** Transverse and **(b)** longitudinal virtual slices of segmented vascular porosities in neutron data masked with X-ray data segmentation. Scale bar equals 1 mm and gray level ranges from -4 cm^{-1} to 8 cm^{-1}. **(c)** Rendering of filtered neutron microscopy data masked with X-ray data segmentation. **(d)** Transverse and **(e)** longitudinal virtual slices of segmented bone in neutron data masked with X-ray data. Gray level ranges from -4 cm^{-1} to 8 cm^{-1}. **(f)** Rendering of filtered neutron microscopy bone data masked with X-ray data. **(g)** Histogram of the neutron gray levels of the vascular porosities in neutron data masked with X-ray data in light gray using left *y*-axis and of the bone in the neutron data in dark gray using right *y*-axis. Bin width is 0.05 in both cases.

measures to preserve the deuteration state. In addition, this testifies to the possibility of separating air, bone, and H_2O using segmentation of the neutron data only, but as the histogram peaks overlap (Fig. 4g), the segmentation might not be easy, which is also evident from the previous sections. Thus, correlative information is advantageous, as the X-ray data is easy to segment and enables a segmentation of the three contrasting phases in the neutron data, which elevates the combined analysis.

A main point of this study is the high neutron data quality with a voxel size of 2.7 μm. To emphasize this, both the resolution and contrast in the images are examined. The resolution of the neutron images is found to be 16.14 ± 7.53 μm (see Supplementary Fig. 3). In order to investigate the contrast between the different material phases in the filtered neutron microscopy data, the contrast-to-noise ratio (CNR) was calculated following the procedure of Törnquist et al. [13,20] with $CNR = \frac{|\text{mean}(S_1) - \text{mean}(S_2)|}{\sqrt{\text{std}(S_1)^2 + \text{std}(S_2)^2}}$ where $S_{i=1,2}$ is the gray level distributions of the contrasting phases (Table 1). Since H_2O has the highest intensity and the air/background has the lowest intensity in the data, it is reasonable that the highest CNR is found between these two. The CNR for bone against air/background and for H_2O against bone, are lower and nearly the same, respectively, indicating that bone pores would appear with both air and H_2O as background. Since the CNR for H_2O against bone is lowest of the two, H_2O slightly reduces the contrast in the data. However, the CNR for bone against air/background in the X-ray is unmatched. It should be remembered that the X-ray data is manually scaled through the choice of gray level window of data to be reconstructed. Nevertheless, the CNR for H_2O or organic matter against air/background in the X-ray data is low compared to the CNR for bone against air/background. This indicates the advantage of using both X-rays and neutrons in this case.

To analyze the contrast in the data further, the mean of 10 lines through a virtual slice in the neutron microscopy data is plotted (Fig. 5). As is evident from the histograms (Fig. 4d), the air has the lowest intensity, the H_2O has the highest intensity, while the bone has an intermediate intensity. For comparison, the mean of 10 lines though the same virtual slice in the X-ray data is also plotted in Fig. 5. The X-ray data have much higher intensity values that the neutron data. As air and H_2O has similar, low X-ray absorption values, the plot reveals the position of the pores in the bone. As the CNR values hinted at, the two peaks of H_2O to the right in Fig. 5 (blue arrows) has a lower absolute amplitude than the two air peaks to the left (green arrows), showing again, that the H_2O marginally reduces the contrast in the images. Nevertheless, the contrast between H_2O and air is high in the neutron data, indicating that H_2O is a good candidate as a contrast agent for investigating liquid transport in the vascular canals of bone in radiography mode and possibly in 3D in the future even if acquisition times are currently playing against this.

4. Discussion

In the present work, a single bone sample was imaged with both neutron and X-ray microscopy using near-equivalent voxel sizes to

enable a correlative study. The use of a 2.7 μm voxel size allowed mapping of the vascular spaces in the sample in contrast to previous neutron imaging results [13,16,20,21]. The segmented X-ray data were used as a mask to isolate vascular porosities in the neutron data to afford improved segmentation of the neutron data and enable differentiating H_2O-filled and empty pore spaces (Fig. 4g).

The analysis showed that, within the resolution of the experiment, the H_2O was restricted to the vascular network in the bone (Fig. 4). Additionally, when H_2O is overly abundant, like in the porosities, the contrast between bone and H_2O was reduced compared to air *vs* bone. Even if the H_2O and bone peaks in the gray level histogram overlap, application of morphological operations allows for segmenting air, bone, and H_2O. In a previous study [19], the D_2O was used as a contrast agent for an *in-situ* experiment and then isotope exchanged to H_2O. Even though it reduced the contrast slightly compared to air, H_2O can still be considered as a good candidate for *in-situ* measurements, as it has a higher neutron attenuation than both air and bone, enabling a separation of all three phases. Most likely, D_2O would have performed in a comparable manner. However, using D_2O as a way to hydrate bone samples before mechanical testing, the hydration protocol is key, as described by Törnquist et al [20] They soaked bone in salinized D_2O (0.9 % NaCl), while we pumped D_2O through the sample. The soaking applied by Törnquist et al. may lead to partial deuteration of the bone matrix, which was avoided by the protocol applied in the present study. Insufficient hydration of bone samples can be detrimental to the analysis and reduce the contrast to a point where it is difficult to image the trabecular structures of the bone [20]. Both for D_2O-soaked bone with reduced contrast and for *in-situ* flow experiments with D_2O, correlative studies with two modalities would prove useful. The present data highlights differences between neutrons and X-rays, as the neutrons clearly capture the liquid as something different from bone and can differentiate D_2O and H_2O, whereas X-rays is unable to distinguish D_2O, H_2O, and organic matter in the presence of the high contrast mineralized bone matrix. In contrast, X-rays catch the mineralization differences between osteonal and interstitial bone well, while the neutrons are less sensitive to the concentration of these heavy elements (Ca and P). Hence, both modalities have their strengths and weaknesses, and by combining them, the "best of both worlds" can be achieved. However, it should be noted that the X-ray data only shows mineralization differences because we applied long exposure times resulting in a measurement time of ~26 h. A standard lab-based μCT measurement would normally only take a couple of hours, but will result in little to no visual difference between osteonal and interstitial bone. Since the Neutron Microscope detector can reach a spatial resolution below 5 μm [24], as the leading instrument in its field [24], extensive X-ray measurements are appropriate.

In order to obtain the benefits of bi-modal X-ray and neutron imaging at the same instrument or even at the same time, some places offer X-ray imaging within the neutron beamline. This is true for both NEUTRA [37] and the neutron imaging instrument ICON at the Paul Scherrer Institute (PSI) in Villigen, Switzerland [38]. Corresponding options have meanwhile also been implemented at the NeXT instrument at Institut Laue-Langvin (ILL) in Grenoble, France [39] and the NeXT system at the National Institute of Standards and Technology (NIST), Gaithersburg, MA, USA [40]. Measuring the neutron and X-ray data simultaneously means that the acquisition time for such a complementary dataset would significantly decrease, making bi-modal X-ray and neutron imaging a relevant option. As the sample is fixed in space in these facilities, relatively little post-processing is needed to register the two datasets, compared to the present study where the sample is mounted and measured twice. Further developments in this neutron-X-ray tomography field would be beneficial, both in regards to image registration and resolution. An analogous case is PET-CT, where a PET (positron emission tomography) and a CT (computed tomography) scanner are combined into one instrument reaping the benefit of both imaging modalities.

An alternative route to take, would be improving post-processing in

Table 1
Contrast-to-noise ratio for different contrasting material phases in the filtered neutron microscopy data and for the X-ray data, respectively.

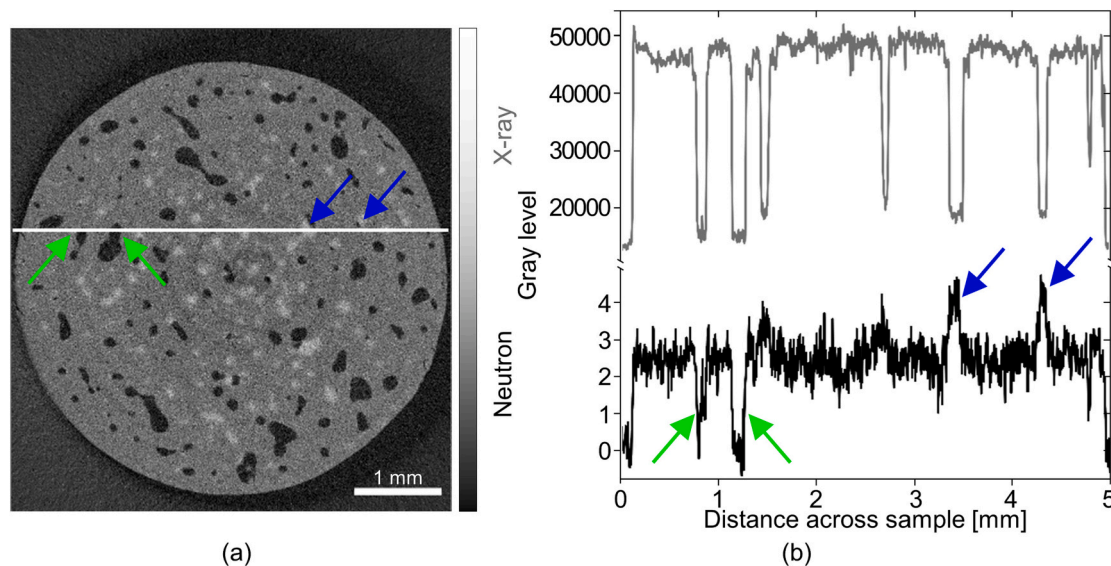| Contrasting material phases	CNR
Filtered neutron data	
H_2O *vs* air/background	2.54
Bone *vs* air/background	1.60
H_2O *vs* bone	1.03
X-ray data	
Bone *vs* air/background	9.94
H_2O/organic *vs* air/background	1.81

Fig. 5. Line plot across sample **(a)** Virtual neutron slice with line in question marked. Green arrows indicate empty pores and blue arrows indicate H_2O filled pores. Scale bar equals 1 mm and gray level ranges from -4 cm^{-1} to 8 cm^{-1}. **(b)** Mean of 10 lines across virtual slice (five above and four below line depicted in (a)) in both neutron (bottom) and X-ray (top) microscopy data. Green arrows indicate empty pores and blue arrows indicate H_2O filled pores. (For interpretation of the references to color in this figure legend, the reader is referred to the web version of this article.)

software for example using digital volume correlation (DVC) algorithms to register two datasets with different modalities even though it is mostly used for *in-situ* analyses and 4D time-lapse data [41–43]. By automating the post-processing, the utilization of neutron micro-tomography in combination with a lab-based X-ray micro-tomography would be an efficient approach [44]. Digital volume correlation methods applied to lower resolution data or radiographies may also be beneficial for future *in situ* neutron imaging experiments to follow the liquid transport in bone [14,15]. However, the present study clearly shows that even without optimized post-processing algorithms, the methodology is already very powerful.

5. Conclusion

A correlative study was performed using 3D neutron and X-ray microscopy on a bone sample infused with D_2O using a 2.7 μm voxel size to enable 3D mapping of vascular porosities in bone. Segmentations of the two modalities showed clear differences, as the neutrons were able to image the liquid, while the vascular porosities were clearly distinguishable with both modalities, where X-ray microscopy provided higher resolution and signal-to-noise ratio. Hence, each modality has its advantage and when using a material that look different in the two modalities, like D_2O or H_2O, one can achieve the best of both worlds by combining the complementary information obtained from each dataset. When segmenting the neutron data using the X-ray data it was possible to localize the liquid in the vascular porosities of the bone sample and determine that the infused D_2O had isotope exchanged to H_2O. Furthermore, there were no indication of H_2O had permeated into the bone matrix. The neutron contrast of pores was reduced when these were filled with H_2O compared to air. As H_2O is very distinct in the neutron data and as D_2O, H_2O, and organic matter can barely be distinguished from air in the X-ray data, the complementary use of both X-rays and neutrons is very favorable.

CRediT authorship contribution statement

Maja Østergaard: Conceptualization, Formal analysis, Investigation, Visualization, Writing – original draft, Writing – review & editing. **Estrid Buhl Naver:** Investigation, Writing – review & editing. **Delia Schüpbach:** Investigation, Writing – review & editing. **Anders Kaestner:** Investigation, Writing – review & editing. **Markus Strobl:** Investigation, Writing – review & editing. **Annemarie Brüel:** Resources, Writing – review & editing. **Jesper Skovhus Thomsen:** Resources, Writing – review & editing. **Søren Schmidt:** Investigation, Writing – review & editing. **Henning Friis Poulsen:** Funding acquisition, Writing – review & editing. **Luise Theil Kuhn:** Supervision, Writing – review & editing. **Henrik Birkedal:** Conceptualization, Formal analysis, Funding acquisition, Supervision, Writing – original draft, Writing – review & editing.

Declaration of competing interest

None.

Data availability

Data are available at https://doi.org/10.5281/zenodo.7743859, this is stated in the manuscript.

Acknowledgements

Appendix A. Supplementary data

Supplementary data to this article can be found online at https://doi.org/10.1016/j.bone.2023.116837.

References

[1] M.E. Launey, M.J. Buehler, R.O. Ritchie, On the mechanistic origins of toughness in bone, Annu. Rev. Mater. Sci. 40 (1) (2010) 25–53, https://doi.org/10.1146/annurev-matsci-070909-104427.

[2] N. Reznikov, M. Bilton, L. Lari, M.M. Stevens, R. Kröger, Fractal-like hierarchical organization of bone begins at the nanoscale, Science 360 (6388) (2018), https://doi.org/10.1126/science.aao2189 p. eaao2189.

[3] N. Reznikov, J.A.M. Steele, P. Fratzl, M.M. Stevens, A materials science vision of extracellular matrix mineralization, Nat. Rev. Mater. 1 (8) (2016) 16041, https://doi.org/10.1038/natrevmats.2016.41.

[4] U.G.K. Wegst, H. Bai, E. Saiz, A.P. Tomsia, R.O. Ritchie, Bioinspired structural materials, Nat. Mater. 14 (1) (2015) 23–36, https://doi.org/10.1038/nmat4089.

[5] S. Weiner, H.D. Wagner, The material bone: structure-mechanical function relations, Annu. Rev. Mater. 28 (1) (1998) 271–298, https://doi.org/10.1146/annurev.matsci.28.1.271.

[6] N.K. Wittig, H. Birkedal, Bone hierarchical structure: spatial variation across length scales, Acta Crystallogr. B 78 (3) (2022), https://doi.org/10.1107/S2052520622001524.

[7] N.K. Wittig, M. Laugesen, M.E. Birkbak, F.L. Bach-Gansmo, A. Pacureanu, S. Bruns, M.H. Wendelboe, A. Brüel, H.O. Sørensen, J.S. Thomsen, H. Birkedal, Canalicular junctions in the osteocyte lacuno-canalicular network of cortical bone, ACS Nano 13 (6) (2019) 6421–6430, https://doi.org/10.1021/acsnano.8b08478.

[8] S.P. Fritton, S. Weinbaum, Fluid and solute transport in bone: flow-induced mechanotransduction, Annu. Rev. Fluid Mech. 41 (1) (2009) 347–374, https://doi.org/10.1146/annurev.fluid.010908.165136.

[9] M.T. Sánchez, M.Á. Pérez, J.M. García-Aznar, The role of fluid flow on bone mechanobiology: mathematical modeling and simulation, Comput. Geosci. 25 (2) (2021) 823–830, https://doi.org/10.1007/s10596-020-09945-6.

[10] D.A. Monteiro, N.S. Dole, J.L. Campos, S. Kaya, C.A. Schurman, C.D. Belair, T. Alliston, Fluid shear stress generates a unique signaling response by activating multiple TGFβ family type I receptors in osteocytes, FASEB J. 35 (3) (2021), e21263, https://doi.org/10.1096/fj.202001998R.

[11] F. Guillaume, S. Le Cann, A. Tengattini, E. Törnquist, C. Falentin-Daudre, H. Albini Lomami, Y. Petit, H. Isaksson, G. Haïat, Neutron microtomography to investigate the bone-implant interface—comparison with histological analysis, Phys. Med. Biol. 66 (10) (2021), 105006, https://doi.org/10.1088/1361-6560/abf603.

[12] H. Isaksson, S. Le Cann, C. Perdikouri, M.J. Turunen, A. Kaestner, M. Tägil, S.A. Hall, E. Tudisco, Neutron tomographic imaging of bone-implant interface: comparison with X-ray tomography, Bone 103 (2017) 295–301, https://doi.org/10.1016/j.bone.2017.07.022.

[13] E. Törnquist, S. Le Cann, E. Tudisco, A. Tengattini, E. Andò, N. Lenoir, J. Hektor, D.B. Raina, M. Tägil, S.A. Hall, H. Isaksson, Dual modality neutron and x-ray tomography for enhanced image analysis of the bone-metal interface, Phys. Med. Biol. 66 (13) (2021), 135016, https://doi.org/10.1088/1361-6560/ac02d4.

[14] N. Kardjilov, I. Manke, R. Woracek, A. Hilger, J. Banhart, Advances in neutron imaging, Mater. Today 21 (6) (2018) 652–672, https://doi.org/10.1016/j.mattod.2018.03.001.

[15] A. Tengattini, N. Lenoir, E. Andò, G. Viggiani, Neutron imaging for geomechanics: a review, Geomech. Energy Environ. 27 (2021), 100206, https://doi.org/10.1016/j.gete.2020.100206.

[16] A. Silveira, N. Kardjilov, H. Markötter, E. Longo, I. Greving, P. Lasch, R. Shahar, P. Zaslansky, Water flow through bone: neutron tomography reveals differences in water permeability between osteocytic and anosteocytic bone material, Mater. Des. 224 (2022), 111275, https://doi.org/10.1016/j.matdes.2022.111275.

[17] B. Cordonnier, A. Pluymakers, A. Tengattini, S. Marti, A. Kaestner, F. Fusseis, F. Renard, Neutron imaging of cadmium sorption and transport in porous rocks, Front. Earth Sci. 7 (306) (2019), https://doi.org/10.3389/feart.2019.00306.

[18] M. Zarebanadkouki, P. Trtik, F. Hayat, A. Carminati, A. Kaestner, Root water uptake and its pathways across the root: quantification at the cellular scale, Sci. Rep. 9 (1) (2019) 12979, https://doi.org/10.1038/s41598-019-49528-9.

[19] M. Østergaard, E.B. Naver, A. Kaestner, P.K. Willendrup, A. Brüel, H.O. Sørensen, J.S. Thomsen, S. Schmidt, H.F. Poulsen, L.T. Kuhn, H. Birkedal, Polychromatic neutron phase contrast imaging of weakly absorbing samples enabled by phase retrieval, J. Appl. Crystallogr. 56 (2023) 673–682, https://doi.org/10.1107/S1600576723003011.

[20] E. Törnquist, S. Le Cann, A. Tengattini, L. Helfen, J. Kok, S.A. Hall, H. Isaksson, The hydration state of bone tissue affects contrast in neutron tomographic images, Front. Bioeng. Biotechnol. 10 (2022), 911866, https://doi.org/10.3389/fbioe.2022.911866.

[21] D. Schwarz, P. Vontobel, E.H. Lehmann, C.A. Meyer, G. Bongartz, Neutron tomography of internal structures of vertebrate remains: a comparison with X-ray computed tomography, Palaeontol. Electron. 8 (2) (2005) 30A.

[22] C. Zanolli, B. Schillinger, O. Kullmer, F. Schrenk, J. Kelley, G.E. Rössner, R. Macchiarelli, When X-rays do not work. Characterizing the internal structure of fossil hominid dentognathic remains using high-resolution neutron microtomographic imaging, Front. Ecol. Evol. 8 (2020) 42, https://doi.org/10.3389/fevo.2020.00042.

[23] M. Granke, M.D. Does, J.S. Nyman, The role of water compartments in the material properties of cortical bone, Calcif. Tissue Int. 97 (3) (2015) 292–307, https://doi.org/10.1007/s00223-015-9977-5.

[24] P. Trtik, E.H. Lehmann, Progress in high-resolution neutron imaging at the Paul Scherrer Institut - the neutron microscope project, J. Phys. Conf. Ser. 746 (1) (2016), 012004, https://doi.org/10.1088/1742-6596/746/1/012004.

[25] A.P. Kaestner, S. Hartmann, G. Kühne, G. Frei, C. Grünzweig, L. Josic, F. Schmid, E.H. Lehmann, The ICON beamline – a facility for cold neutron imaging at SINQ, NIM-A 659 (1) (2011) 387–393, https://doi.org/10.1016/j.nima.2011.08.022.

[26] P. Boillat, C. Carminati, F. Schmid, C. Grünzweig, J. Hovind, A. Kaestner, D. Mannes, M. Morgano, M. Siegwart, P. Trtik, P. Vontobel, E.H. Lehmann, Chasing quantitative biases in neutron imaging with scintillator-camera detectors: a practical method with black body grids, Opt. Express 26 (12) (2018) 15769–15784, https://doi.org/10.1364/OE.26.015769.

[27] C. Carminati, P. Boillat, F. Schmid, P. Vontobel, J. Hovind, M. Morgano, M. Raventos, M. Siegwart, D. Mannes, C. Gruenzweig, P. Trtik, E. Lehmann, M. Strobl, A. Kaestner, Implementation and assessment of the black body bias correction in quantitative neutron imaging, PLoS ONE 14 (1) (2019), e0210300, https://doi.org/10.1371/journal.pone.0210300.

[28] A.P. Kaestner, MuhRec—a new tomography reconstructor, NIM-A 651 (1) (2011) 156–160, https://doi.org/10.1016/j.nima.2011.01.129.

[29] B. Münch, P. Trtik, F. Marone, M. Stampanoni, Stripe and ring artifact removal with combined wavelet — Fourier filtering, Opt. Express 17 (10) (2009) 8567–8591, https://doi.org/10.1364/OE.17.008567.

[30] M. Burger, G. Gilboa, S. Osher, J. Xu, Nonlinear inverse scale space methods, Commun. Math. Sci. 1 (1) (2006) 179–212, https://doi.org/10.4310/CMS.2006.v4.n1.a7.

[31] C. Carminati, M. Strobl, A. Kaestner, KipTool, a general purpose processing tool for neutron imaging data, SoftwareX 10 (2019), 100279, https://doi.org/10.1016/j.softx.2019.100279.

[32] N.K. Wittig, M. Østergaard, J. Palle, T.E.K. Christensen, B.L. Langdahl, L. Rejnmark, E.-M. Hauge, A. Brüel, J.S. Thomsen, H. Birkedal, Opportunities for biomineralization research using multiscale computed X-ray tomography exemplified by bone imaging, J. Struct. Biol. 214 (1) (2022), 107822, https://doi.org/10.1016/j.jsb.2021.107822.

[33] N.K. Wittig, J. Palle, M. Østergaard, S. Frølich, M.E. Birkbak, K.M. Spiers, J. Garrevoet, H. Birkedal, Bone biomineral properties vary across human osteonal bone, ACS Nano 13 (11) (2019) 12949–12956, https://doi.org/10.1021/acsnano.9b05535.

[34] J.K. Im, L. Jeong, J. Crha, P. Trtik, J. Jeong, High-resolution neutron imaging reveals kinetics of water vapor uptake into a sessile water droplet, Matter 4 (6) (2021) 2083–2096, https://doi.org/10.1016/j.matt.2021.04.013.

[35] N. Ott, C. Cancellieri, P. Trtik, P. Schmutz, High-resolution neutron imaging: a new approach to characterize water in anodic aluminum oxides, Mater. Today Adv. 8 (2020), 100121, https://doi.org/10.1016/j.mtadv.2020.100121.

[36] J. Terreni, M. Trottmann, R. Delmelle, A. Heel, P. Trtik, E.H. Lehmann, A. Borgschulte, Observing chemical reactions by time-resolved high-resolution neutron imaging, J. Phys. Chem. C 122 (41) (2018) 23574–23581, https://doi.org/10.1021/acs.jpcc.8b07321.

[37] E.H. Lehmann, D. Mannes, A.P. Kaestner, J. Hovind, P. Trtik, M. Strobl, The XTRA option at the NEUTRA facility—more than 10 years of bi-modal neutron and X-ray imaging at PSI, Appl. Sci. 11 (9) (2021) 3825, https://doi.org/10.3390/app11093825.

[38] A.P. Kaestner, J. Hovind, P. Boillat, C. Muehlebach, C. Carminati, M. Zarebanadkouki, E.H. Lehmann, Bimodal imaging at ICON using neutrons and X-rays, Phys. Procedia 88 (2017) 314–321, https://doi.org/10.1016/j.phpro.2017.06.043.

[39] A. Tengattini, N. Lenoir, E. Andò, B. Giroud, D. Atkins, J. Beaucour, G. Viggiani, NeXT-Grenoble, the neutron and X-ray tomograph in grenoble, NIM-A 968 (2020), 163939, https://doi.org/10.1016/j.nima.2020.163939.

[40] J.M. LaManna, D.S. Hussey, E. Baltic, D.L. Jacobson, Neutron and X-ray Tomography (NeXT) system for simultaneous, dual modality tomography, Rev. Sci. Instrum. 88 (11) (2017), 113702, https://doi.org/10.1063/1.4989642.

[41] A. Buljac, C. Jailin, A. Mendoza, J. Neggers, T. Taillandier-Thomas, A. Bouterf, B. Smaniotto, F. Hild, S. Roux, Digital volume correlation: review of progress and challenges, Exp. Mech. 58 (5) (2018) 661–708, https://doi.org/10.1007/s11340-018-0390-7.

[42] E. Tudisco, C. Jailin, A. Mendoza, A. Tengattini, E. Andò, S.A. Hall, G. Viggiani, F. Hild, S. Roux, An extension of digital volume correlation for multimodality image registration, Meas. Sci. Technol. 28 (9) (2017), 095401, https://doi.org/10.1088/1361-6501/aa7b48.

[43] O. Stamati, E. Andò, E. Roubin, R. Cailletaud, M. Wiebicke, G. Pinzon, C. Couture, R. Hurley, R. Caulk, D. Caillerie, Spam: software for practical analysis of materials, J. Open Source Softw. 5 (51) (2020) 2286, https://doi.org/10.21105/joss.02286.

[44] P. Trtik, Neutron microtomography of voids in gold, MethodsX 4 (2017) 492–497, https://doi.org/10.1016/j.mex.2017.11.009.